Temporal interferences driven by a single-cycle terahertz pulse in the photodetachment dynamics of negative ions

B. C. Yang and F. Robicheaux

Temporal interferences driven by a single-cycle terahertz pulse in the photodetachment dynamics of negative ions

B. C. Yang and F. Robicheaux*

Department of Physics and Astronomy, Purdue University, West Lafayette, Indiana 47907, USA

We present theory and calculations of a real-time-domain interferometry for the photodetachment dynamics of negative ions in the presence of a single-cycle terahertz pulse. The photoelectron can follow two or more classical trajectories to arrive at a detector *simultaneously* allowing the electron waves to interfere quantum mechanically. Both the inphase and antiphase oscillations can be observed in the photoelectron interferences from negative hydrogen and fluorine ions depending on the pulse strength and the observing angle. Especially, a temporal-caustic bifurcation is observed when the detection angle is not in the line with the pulse polarization direction. Similar interferences and bifurcations are also expected in the angle-resolved energy spectrum, as a result of its approximate equivalence with the time-dependent electron flux at large distances.

I. INTRODUCTION

One of the significant achievements in terahertz (THz) techniques is the routine generation of a single-cycle THz pulse, representing a limiting oscillation cycle of the electric field in a propagating pulse. Compared with the more usual multi-cycle pulses, it has several fundamentally different but useful characteristics, including a different energy-transfer mechanism, a non-zero spatial displacement of a free charge, and also a one-directional momentum transfer. For example, single-cycle THz pulses have found applications in manipulating the alignment and orientation of polar molecules[1, 2]. Recently, they have also been used to explore the field ionization of Rydberg atoms, where a new threshold behavior was discovered along with other interesting phenomena[3–5]. Here, we demonstrate its possible applications in modulating and controlling the photodetachment dynamics of negative ions by analyzing the electron dynamics and the temporal interferences caused by a single-cycle pulse.

The present idea of applying a single-cycle THz pulse in the photodetachment process originates from traditional photodetachment microscopy which has been and is still the most accurate instrument for measuring the atomic affinity. In photodetachment microscopy[6, 7], a static electric field is used to project the photoelectron towards a detector located at a macroscopic distance ($\sim 0.5m$) from the photodetachment zone. A spatial interference pattern can be observed on the detector and can be interpreted as quantum interferences between electron waves propagated along different classical trajectories[8–10]. A similar idea has also been implemented for neutral atoms, known as photoionization microscopy[11]. These direct-imaging techniques have achieved great successes in recent years for visualizing the electron wave function in atoms or ions[12–14]. In contrast with traditional photodetachment (or photoionization) microscopy with a static electric field, the current availability of a single-cycle pulse provides an opportunity to observe electron interferences in the real time domain. In this work, we only focus on the photodetachment dynamics of negative ions. For the photoionization of neutral atoms, the essential physical picture is similar, and the theoretical methods developed here can be easily extended by including the long-range Coulomb potential.

As illustrated in Fig. 1 for a weak single-cycle pulse, there are two trajectories contributing to each time t_f when the electron arrives at the detector. One is generated earlier in the photodetachment process and the other later, indicated by the dotted lines in Fig. 1(a) and (b). The associated electron waves interfere with each other as a result of the different quantum phases accumulated by the electron moving along these two trajectories. Two examples of the interference pattern are shown in Fig. 1(c) and (d), respectively, for the hydrogen (H^-) and fluorine (F^-) negative ions. Moreover, the amplitude of a single-cycle THz pulse can easily reach several tens of kV/cm in a table-top experiment. With a stronger driving pulse, the electron dynamics becomes more complicated but much more interesting: more than two trajectories may arrive at a detecting point simultaneously, and the temporal caustic as in Fig. 1(a) experiences a bifurcation by varying the observing angle. As a consequence, both the inphase and antiphase oscillations can be observed between the temporal interference spectra from H^- and F^-, reflecting the different angular distribution of the initially outgoing electron wave.

Furthermore, our studies may also provide further insight in understanding the electron dynamics in an intense driving laser field which is usually encountered in strong field and ultrafast physics. In our present system, the electron is ejected from a negative ion by absorbing one photon from a weak laser field while, in strong field and ultrafast physics, the initial electron wave is usually generated through the strong-field tunneling process[15], or launched by a series of attosecond pulses[16], or just
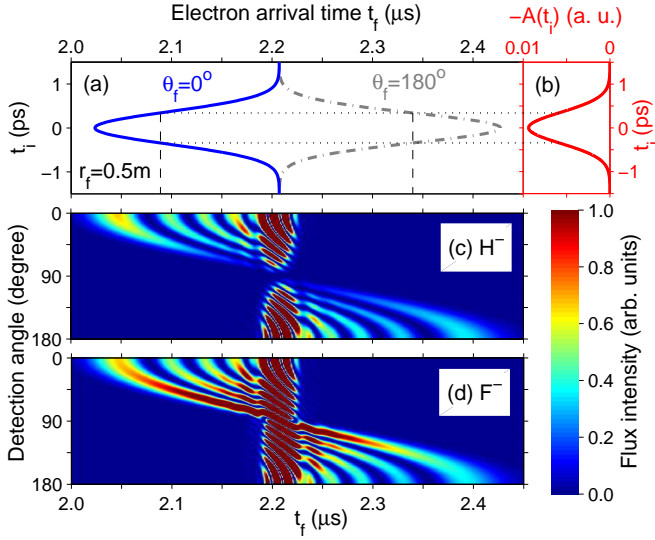
FIG. 1: (Color online) Demonstration of the temporal interferences caused by a single-cycle THz pulse with a maximum field strength of $2kV/cm$. (a) t_f vs t_i with t_f defined as the time when the electron arrives at a detector located at $(r_f = 0.5m, \theta_f)$. (b) The unipolar momentum transfer from the THz pulse to an electron generated at a certain initial time t_i in the photodetachment process. The detection angle θ_f could be changed as in the graph, and the angle-resolved interference patterns are shown in (c) and (d) for H^- and F^-, respectively, from quantum simulations with the electron initial kinetic energy $E_0 \approx 0.1454eV$. The relative intensity of the electron flux is given by a color bar in the right bottom.
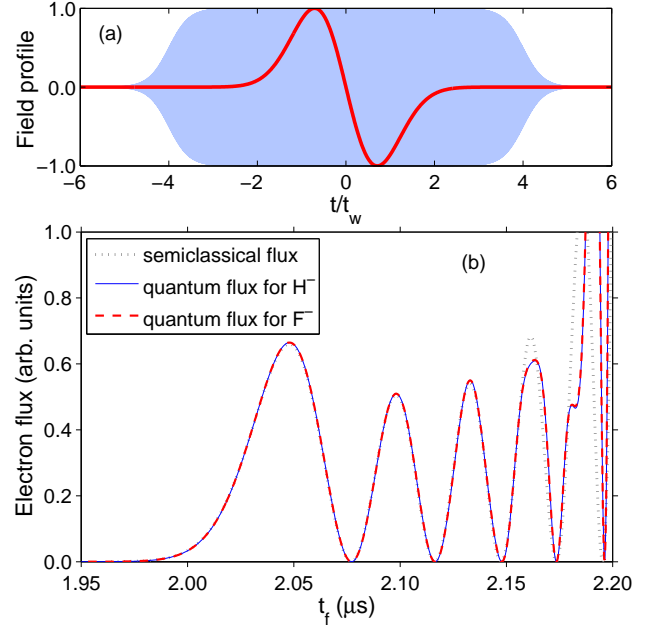

FIG. 2: (Color online) (a) Field configurations for the present system. The gray curve and the solid red line represent the weak laser field and the single-cycle THz pulse, respectively, divided by their corresponding field amplitudes. $t_w = 0.5ps$. The oscillation feature of the laser field is not distinguishable as a result of its much higher frequency than the THz pulse. (b) Example calculations for the time-dependent electron flux, corresponding to the interferences shown in Fig. 1(c) and (d) with $\theta_f = 0$. The dotted line is calculated by the semiclassical propagation method. The solid and the dashed curves are computed by directly solving the time-dependent Shrödinger equations for H^- and F^-, respectively.

using an ultrashort electron pulse[17]. However, except for the details of various electron sources, the subsequent electron propagation after its generation is quite similar between different systems, mainly determined by the time-dependent vector potential of the driving field. The semiclassical formulae used in the present work allow us to propagate the electron wave exactly following classical trajectories in the augmented phase space, thus providing a clear physical picture for the embedded electron dynamics in the temporal interference spectra. The semiclassical spectra calculated in this way are quantitatively accurate as verified by comparing with quantum simulations. Although the time-dependent electron flux is specifically calculated in our current work, it is established that the temporal flux at large distances is approximately equivalent to the angle-resolved energy spectrum.

The remainder of this paper is organized as follows. In Sec. II, we give a brief description of the photoelectron generation process, and discuss the different classical electron dynamics expected in the single-cycle driving field. In Sec. III, both the quantum and semiclassical propagation methods are described in detail. The different temporal interference structures are analyzed in Sec. IV, as well as the temporal-caustic bifurcation and its related physical observations. A brief conclusion is given in Sec. V. Atomic units are used throughout this work

unless specified otherwise.

II. ELECTRON DYNAMICS

A. Photoelectron generation by a weak laser field

The considered atomic negative ion (H^- or F^-) is interacting simultaneously with a weak laser field and an additional single-cycle driving pulse. Since the electric field of the single-cycle pulse varies much slower than the detachment laser field(Fig. 2(a)), the whole photodetachment process can be approximately divided into two steps: first, the photoelectron is generated from the negative ion by absorbing one photon from the laser field, and then the subsequent electron dynamics will be dominated by the single-cycle THz pulse. In addition, the currently available single-cycle pulse as in Ref. [3] is too weak to do anything to a negative ion in the ground state. However, it can strongly modify the electron dynamics once the electron is launched into the continuum by a weak laser. In this subsection, we first outline several theoretical aspects related to the initially photoelectron

generation process in a weak laser field.

The theoretical model has been well established for one-photon photodetachment by a weak laser field[10, 18]. The generated electron wave at an initial time t_i can be formally written as $\psi(\mathbf{r}, t_i) = \psi_{out}(\mathbf{r}) \exp(-iE_0 t_i)$ with the time-independent part $\psi_{out}(\mathbf{r})$ satisfying the following inhomogeneous Schrödinger equation,

$$(E_0 - H_a)\psi_{out}(\mathbf{r}) = D\varphi_i \ , \tag{1}$$

where E_0 denotes the photoelectron initial kinetic energy, and D is the dipole operator. For the linearly-polarized laser along the z-axis, $D = z$. H_a is the atomic Hamiltonian including the short-range potential, and φ_i represents the initial bound state. The electron goes into a spherically outgoing wave,

$$\psi_{out}(R, \theta_i, \phi_i) = C(k_0) Y_{lm}(\theta_i, \phi_i) \frac{e^{ik_0 R}}{R} \ , \tag{2}$$

when the radius R satisfies

$$\frac{1}{\sqrt{2E_0}} \ll R \ll \frac{E_0}{F_m} \tag{3}$$

with F_m denoting the field amplitude of an applied single-cycle pulse. The right-hand side restriction in Eq. (3) is added by considering an applied external field like a single-cycle pulse interested here, which requires the applied field strength F_m to be not larger than $k_0^3/2$ with $k_0 = \sqrt{2E_0}$, therefore guaranteeing that the external field does not distort the initially outgoing wave obviously. R, θ_i and ϕ_i in Eq. (2) are spherical coordinates of the electron relative to the rest atom; $C(k_0)$ is a complex coefficient dependent on the photoelectron energy E_0, and $Y_{lm}(\theta_i, \phi_i)$ is the spherical harmonic function representing the initial angular distribution of the generated electron wave. The photodetachment of H^- gives an outgoing p-wave with $l = 1$ and $m = 0$, while the photodetachment of F^- generates an s-wave with $l = 0$ and $m = 0$, where the d-wave is largely suppressed according to the Wigner power law near the photodetachment threshold[19]. Note that the applied laser has been assumed to be linearly polarized along z-axis.

Since our motivation is to study the temporal interferences induced by a single-cycle THz pulse, a laser pulse as in Fig. 2(a) is used with a finite duration. In a real experiment, the laser-pulse duration can be longer than that in Fig. 2(a), according to the discussions in the following subsection. For simplicity, we assume the laser field to be turned on and off slowly enough so that the outgoing wave form in Eq. (2) is still a good approximation at each time instant. Under this assumption, the generated outgoing wave at each initial time t_i can be approximately expressed as

$$\psi_0(R, \theta_i, \phi_i, t_i) = f_L(t_i)\psi_{out}(R, \theta_i, \phi_i)e^{-iE_0 t_i} \ , \tag{4}$$

with $f_L(t)$ representing the slowly varying envelope of an applied laser field. Specifically, the following laser field

envelope is used in our calculations,

$$f_L(t) = \frac{1}{2}\left[\tanh\left(\frac{t - t_u}{t_L}\right) - \tanh\left(\frac{t - t_d}{t_L}\right)\right] \ , \tag{5}$$

where $t_u = -2ps$ and $t_d = 2ps$, indicating the time when the laser field is turned on and off, respectively. t_L controls how fast the laser field is turned on and off.

For H^-, we choose the photon energy $\hbar\omega_L = 0.9eV$ and $t_L = 50T_L$, where ω_L and T_L denote the laser frequency and its oscillation period, respectively. The gray curve in Fig. 2(a) depicts the laser pulse divided by its maximum field amplitude. For F^-, the photon energy is chosen to give an equal electron kinetic energy E_0 as for H^-, which makes it possible to compare the final results for the two negative ions. From the model potentials adopted in our quantum simulations (see Sec. III for the details), we obtain the binding energies for H^- and F^- to be 0.02773a.u. and 0.125116a.u., respectively. Therefore, the electron initial kinetic energy $E_0 = 0.1454eV$, and the photon energy for F^- is about $3.55eV$. To make sure the laser field is turned on and off slowly enough, we choose $t_L = 200T_L$ for F^-, and the resulted field envelope is similar to that in Fig. 2(a) for H^-.

B. Electron motion in a single-cycle driving pulse

The applied single-cycle pulse is also assumed to be linearly polarized along the z-axis. The specific profile is constructed by a Gaussian-shape vector potential[4],

$$A(t) = -\frac{F_m t_w}{\sqrt{2}} e^{-\frac{t^2}{t_w^2} + \frac{1}{2}} \ . \tag{6}$$

and its electric field $F(t)$ has the following form

$$F(t) = -\frac{\sqrt{2}F_m t}{t_w} e^{-\frac{t^2}{t_w^2} + \frac{1}{2}} \tag{7}$$

with the field amplitude given by F_m and the pulse duration controlled by t_w. For the THz pulse considered here(Fig. 2(a)), we set $t_w = 0.5ps$. Besides the vector potential and the electric field, the integrals of $A(t)$ and $A^2(t)$ are also two important quantities for completely describing the electron dynamics. They are directly related to the electron spatial displacement and the quantum phase accumulation, respectively. The analytical expressions for these integrals can be found in Appendix A.

Using the cylindric coordinates with the negative ion as its origin, the classical electron motion in the single-cycle driving pulse can be described by the following equations

$$\begin{align}
p_\rho &= k_0 \sin(\theta_i) \tag{8} \\
p_z(t) &= k_0 \cos(\theta_i) + \Delta p_z(t_i, t) \tag{9} \\
\rho(t) &= k_0(t - t_i)\sin(\theta_i) \tag{10} \\
z(t) &= k_0(t - t_i)\cos(\theta_i) + \Delta z(t_i, t) \tag{11}
\end{align}$$

where (p_ρ, ρ) and (p_z, z) represent the electron momenta and coordinates in the separable ρ and z directions, respectively. According to the physical consideration in Eq.(3), a more reasonable starting point for the electron should be $(R\sin(\theta_i), R\cos(\theta_i))$ which has been neglected in Eqs. (10) and (11) because only the electron dynamics at large distances is concerned where the small radius R has negligible effect. The momentum transfer in Eq. (9) comes from the change of the field vector potential,

$$\Delta p_z(t_i, t) = A(t) - A(t_i) , \qquad (12)$$

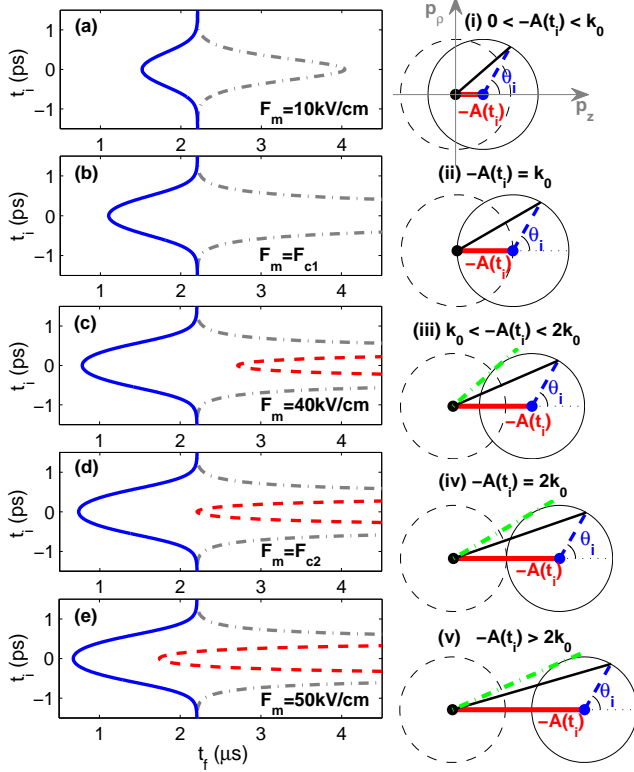which approaches a constant $-A(t_i)$ and only depends

FIG. 3: (Color online) (a)-(e) Electron arrival-time plots with different field amplitudes F_m. The solid blue lines, the dot-dashed gray and the dashed red curves correspond to ($\theta_i = 0$, $\theta_f = 0$), ($\theta_i = \pi$, $\theta_f = \pi$) and ($\theta_i = \pi$, $\theta_f = 0$), respectively. (i)-(v) Momentum-space geometry varying with different drift momentum $-A(t_i)$ obtained from the single-cycle pulse. The dashed and the solid circles represent the end points of the initial and final momentum vectors, respectively, with their directions varying from 0 to 2π. The bold red line represents the momentum transfer $-A(t_i)$, and the length of the line indicates the relative value of $-A(t_i)$ compared with the electron initial momentum k_0. The heavy black and the dashed blue lines demonstrate the angle relationship between the final electron-momentum direction and the initial momentum direction. Note that the initial momentum k_0 (the dashed blue line) has been translated from the dashed circle to the solid circle for convenience in displaying. The dot-dashed green lines in (iii)-(v) indicate the maximum angle of the final momentum direction deviating from the z-direction.

on the initial time t_i of photoelectron generation, when t is sufficiently large such as $t > 6t_w$. The field-induced electron displacement in Eq. (11) consists of two parts:

$$\Delta z(t_i, t) = \int_{t_i}^{t} A(t')dt' - A(t_i)(t - t_i) , \qquad (13)$$

where the first part $\int_{t_i}^{t} A(t')dt'$ comes from an accumulation along with the vector-potential variation, and the second part $-A(t_i)(t - t_i)$ is caused by an additional drift momentum $-A(t_i)$ obtained from the field at the initial time t_i. Therefore, Eq. (11) can be rearranged as

$$z(t) = [k_0 \cos(\theta_i) - A(t_i)](t - t_i) + \Delta\widetilde{z}(t_i) \qquad (14)$$

for $t > 6t_w$, where the first-part contribution in Eq. (13) has been approximated as $\Delta\widetilde{z}(t_i) = \int_{t_i}^{\infty} A(t')dt'$ which is valid as long as t is large enough so that the pulse field has gone to zero.

By combining Eq. (10) and Eq. (14), to eliminate θ_i, one can find the following relationship between the initial electron-generation time t_i and the final time t_f to arrive at a detector located at (r_f, θ_f),

$$t_f = t_i + \frac{r_f}{k_0} \cdot \mu(\xi, \zeta, \theta_f) \qquad (15)$$

with $\xi = -A(t_i)/k_0$ and $\zeta = \Delta\widetilde{z}(t_i)/r_f$. The factor μ is an arrival-time modulator caused by the driving pulse, and its specific form is dependent on the value of momentum transfer $-A(t_i)$ relative to the initial momentum k_0 (Appendix A). Various categories for the electron arrival-time plot are illustrated in Fig. 3(a)-(e) with the observing angle θ_f equal either 0 or π, where the spherical detector is assumed to be placed at $r_f = 0.5m$ as in traditional photodetachment microscopy.

From Eq. (10) divided by Eq. (14), one can also reach the following equation

$$\frac{r_f \sin(\theta_f)}{r_f \cos(\theta_f) - \Delta\widetilde{z}(t_i)} = \tan(\theta_{k_f}) = \frac{k_0 \sin(\theta_i)}{k_0 \cos(\theta_i) - A(t_i)} \qquad (16)$$

for the relations among θ_i, θ_f and the final momentum direction θ_{k_f}. The right-hand side of Eq. (16) can be expressed geometrically in the momentum space and Fig. 3(i)-(v) shows all the possible geometries involved in the electron driven process. After a geometry analysis, the initial emission angle θ_i of the classical trajectory arriving at (r_f, θ_f) can be obtained as

$$\theta_i = \theta_{k_f} + \alpha \qquad (17)$$

for $-A(t_i) \leq k_0$, where $\alpha = \arcsin[\xi \sin(\theta_{k_f})]$ and θ_{k_f} is given by the left-hand side of Eq. (16). When $-A(t_i) > k_0$, there are two solutions,

$$\theta_{i<} = \theta_{k_f} + \alpha ; \qquad (18)$$
$$\theta_{i>} = \theta_{k_f} + \pi - \alpha , \qquad (19)$$

corresponds to the two crossings between the heavy black line and the solid circle in Fig. 3(iii)-(v). The subscripts

"$<$" and "$>$" are consistent with the notation in Appendix A, indicating the trajectory with $\theta_{i<}$ arrives at the detector earlier than that with $\theta_{i>}$. In addition, there is a maximum angle θ_f^m the electron can reach (the dot-dashed green line in Fig. 3(iii)-(v)), and its specific form is given by Eqs. (A14) and (A20) in Appendix A.

One immediate observation from Fig. 3 is that all the background electron trajectories hardly driven by the single-cycle pulse appear to arrive at the detector with a same final time around $t_f = 2.21\mu s$. This is guaranteed by the simple linear relationship in Eq. (15). The initial time t_i of electron generation is on the scale of picosecond, while the electron arrival time t_f is on the scale of microsecond ($r_f/k_0 \approx 2.21\mu s$). As long as the driving field is not too weak to influence the electron momentum ($\Delta p_z \gtrsim 0.1k_0$), the variation of t_f is still appreciable on the microsecond scale. Therefore, the arrival-time differences for the background electron trajectories generated at different initial time (picosecond scale) can be hardly distinguishable. In contrast, those trajectories driven by the pulse field can be well separated in the arrival-time plot (microsecond scale), reflecting the vector-potential variation for different initial time. As a consequence, the restriction is loose for the operation duration of the weak laser field which can be longer than $6ps$ in Fig. 2(a).

The various electron dynamics in Fig. 3 differ in the momentum transfer obtained by the electron from the driving pulse compared with its initial momentum obtained from the weak laser field. According to Eq. (6), a maximum momentum

$$-A_{max} = \frac{F_m t_w}{\sqrt{2}} e^{1/2} \qquad (20)$$

can be transferred from the driving pulse to an electron. Note that the single-cycle pulse has a definite direction of momentum transfer. For our choice in Eq. (6), the momentum transfer is always positive. By interacting with the single-cycle pulse, the electron initially ejected along the momentum-transfer direction is accelerated, and will arrive at the detector much earlier than the background electron, which are demonstrated by the heavy solid blue curves in Fig. 3(a)-(e) with $\theta_i = 0$ and $\theta_f = 0$.

However, if the electron was initially moving in the opposite direction of the final momentum transfer, the situation can be more complicated. When $-A_{max} < k_0$, the electron is simply decelerated and arrives at the detector much later than the background electron, demonstrated by the dot-dashed curve in Fig. 3(a) with $\theta_i = \pi$ and $\theta_f = \pi$. The corresponding geometry of the momentum space is given by Fig. 3(i). Assuming $-A_{max} = k_0$ which gives a critical field amplitude $F_m = F_{c1}$ with

$$F_{c1} = \frac{\sqrt{2}k_0}{t_w} e^{-1/2} , \qquad (21)$$

then the electron generated at an initial time t_i corresponding to the maximum momentum transfer will be stopped at $z = \Delta \tilde{z}(t_i)$ forever. For our case, this happens for the electron generated at $t_i = 0$ with an initial angle $\theta_i = \pi$. Therefore, the final time t_f goes to infinity as the electron generation time t_i tends to 0. It is illustrated by the dot-dashed line in Fig. 3(b) (see also Eq. (A21) in Appendix A), and Fig. 3(ii) depicts the corresponding geometry in the momentum space.

With the field amplitude increasing, the maximum momentum transfer will be larger than the initial momentum, and the electron can be finally fold back to the side in the final momentum-transfer direction, which is illustrated by the dashed red curve in Fig. 3(c) with its momentum-space geometry given by Fig. 3(iii). Once $-A_{max} = 2k_0$, another critical field amplitude $F_m = F_{c2}$ is reached which is just twice of the first critical field value F_{c1} in Eq. (21). For this case, the electron generated near $t_i = 0$ with an initial angle $\theta_i \sim \pi$ can reach the detector almost at the same time as the background electron, as shown by the dashed red line in Fig. 3(d), and the initial and final circles in the momentum space will not overlap anymore (Fig. 3(iv)).

If the applied driving field is strong enough so that $-A_{max} > 2k_0$, then the electron dynamics goes into another interesting region. As in Fig. 3(v), the two circles in the momentum space will be completely separated for the momentum transfer $-A(t_i)$ larger than $2k_0$, and even the electron initially moving in the opposite direction with $\theta_i = \pi$ can also reach the detector at $\theta_f = 0$ much earlier than the background electron, as the electron with $\theta_i = 0$ does. Therefore, in the overlapping region for $\theta_f = 0$ in Fig. 3(e), there are four trajectories arriving at the detector simultaneously. The electron wave parts propagating along these trajectories can interfere quantum mechanically, and more interesting phenomena beyond those in Fig. 1 can be expected.

By a closer look at the momentum-space geometries displayed in Fig. 3, one more interesting phenomenon which we call "temporal-caustic bifurcation" can be found as the observing angle approaches $\pi/2$(Fig. 4). The temporal caustics t_f^c in Fig. 3(a)-(e) are those local extrema of t_f, which corresponds to the classical boundary between the dynamically allowed and forbidden regions in the augmented phase space by including the evolution time t and its conjugate momentum p_t [20]. Classical trajectories are reflected near the caustic, and the corresponding quantum wave has a local maximum distribution. All the observed temporal caustics in Fig. 3(a)-(e) are caused by the maximum vector potential of the applied driving pulse. However, another temporal caustic may appear once the electron initial angle θ_i crosses $\pi/2$, indicated by the dot-dashed gray line in Fig. 4(a).

To imagine the involved dynamic picture, one can first fix the angle of the final kinetic momentum k_f in the momentum space as in Fig. 3(i), and then shift the solid circle away from and back to the dashed circle as in Fig. 4(a), following the time-dependent variation of the vector potential $A(t_i)$. During this simple game, the number of possible pairs of θ_i and t_i corresponding to each value of k_f could be counted, which gives an estimation for the number of contributed trajectories as well as the
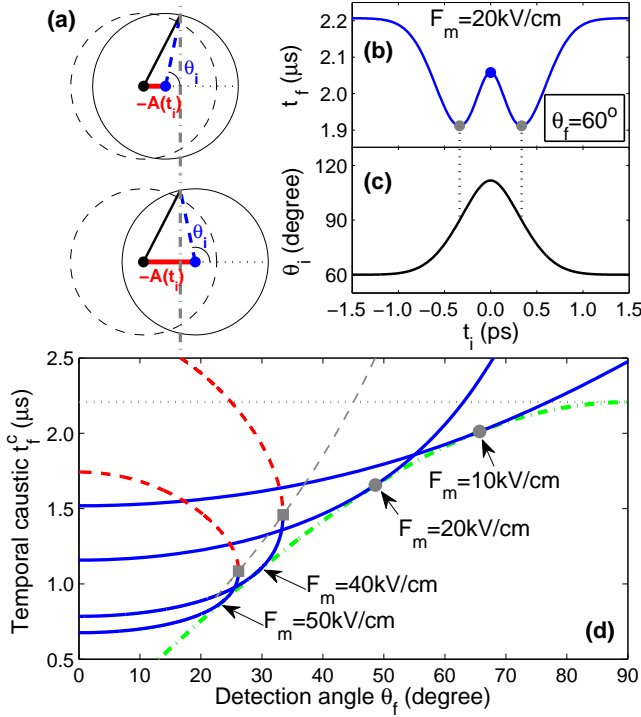
FIG. 4: (Color online) (a) Momentum space geometry after the temporal-caustic bifurcation. The vertical dot-dashed line indicates the corresponding situation of the newly-born caustic. The arrangement for the other lines and colors is the same as in Fig. 3(i)-(v). (b) and (c) display an example of the electron arrival-time plot and its corresponding initial-angle variation. The heavy blue point and two gray points mark, respectively, the temporal caustic with $A(t_i) = A_{max}$ and the newly-born caustic with $\theta_i = \pi/2$. (d) Temporal-caustic variation with different detection angles and applied driving field amplitudes. The dot-dashed green line shows the trace for the bifurcation-point (circle points) shifting with the varying field amplitude, and is also the evolution curve of the newly-born caustic with $\theta_i = \pi/2$ after each bifurcation point. The four demonstrated cases are specified by the text arrows with different field amplitudes, respectively. The heavy blue line and the bold dashed curve depict, respectively, the temporal-caustic dependence on the observing angle θ_f for the same type of line in the arrival-time plot as in Fig. 3(a)-(e). The thin dashed curve shows the variation trace of the joint point (square points) for different field amplitudes. The dotted line indicates the free-electron arrival time t_f without interacting with any external field.

temporal-caustic locations. For a small detection angle θ_f, the temporal caustic t_f^c is the earliest arrival time t_f as in Fig. 3(a), which corresponds to $A(t_i) = A_{max}$ and $\theta_i < \pi/2$. With the observing angle deviating from the field-polarization direction gradually, the corresponding initial angle θ_i also increases.

Once a critical detection angle θ_f^c is reached, the corresponding initial angle will be a right angle with $-A(t_i)$ still the maximum vector potential. This critical case serves as a bifurcation of the temporal caustic. With the

observing angle keeping increasing from θ_f^c, the temporal caustic for $\theta_f = \theta_f^c$ with $A(t_i) = A_{max}$ and $\theta_i = \pi/2$ will split into two caustics, one with $A(t_i) = A_{max}$ and $\theta_i > \pi/2$, the other with $-A(t_i) < -A_{max}$ and $\theta_i = \pi/2$ as in Fig. 4(a). As a result of the unipolar momentum transfer $-A(t_i)$ in a single-cycle pulse, this kind of temporal-caustic bifurcation can only be observed for the final angle $\theta_f < \pi/2$. Figure 4(b) and (c) give an example for the electron arrival-time plot t_f vs t_i in the bifurcation region and its corresponding initial angle θ_i at each initial time t_i, where $F_m = 20kV/cm$ and $\theta_f = \pi/3$. The bifurcated caustics discussed above are marked by the heavy blue point (A_{max}) and the gray points with the dotted guidance lines $(\theta_i = \pi/2)$.

As a brief summary, we present an overall view in Fig. 4(d) for the caustic dependence on the observing angle θ_f and the driving field amplitude F_m. Taking $F_m = 20kV/cm$ for instance, the bifurcation point is displayed by the corresponding circle point, given by

$$\theta_f^b = \arctan(-k_0/A_{max}) ; \qquad (22)$$

$$t_f^b = r_f \sin(\theta_f^b)/k_0 \qquad (23)$$

quantitatively, where the tiny differences of t_i and $\Delta\widetilde{z}(t_i)$ have been neglected. For $\theta_f < \theta_f^b$, there is one temporal caustic following the solid blue curve with its arrival time t_f given by the corresponding solution at $A(t_i) = A_{max}$ in Appendix A. After the bifurcation point, the newly born caustic with $\theta_i = \pi/2$ follows the dot-dashed green curve until $\theta_f = \pi/2$, with its final arrival time t_f given by $r_f \sin(\theta_f)/k_0$ which is invariant for different field amplitudes. For the driving pulse with different field amplitude, the bifurcation point just shifts along the dot-dashed green line according to Eq. (22), and the newly born caustic follows the same dot-dashed curve.

If the driving field is strong enough, another additional temporal caustic will emerge from the fold-back trajectories like those dashed red curves in Fig. 3(c)-(e), which can joint with the above discussed temporal caustic corresponding to $A(t_i) = A_{max}$ after bifurcation point. The joint points are indicated using square points in Fig. 4(d) for $F_m = 40kV/cm$ and $F_m = 50kV/cm$, respectively. The variation trace of this joint point with different field amplitude can be approximately determined by

$$\theta_f^j = \arcsin(-k_0/A_{max}) ; \qquad (24)$$

$$t_f^j = \frac{r_f}{\sqrt{A_{max}^2 - k_0^2}} , \qquad (25)$$

which is depicted by the thin dashed line in Fig. 4(d). After the joint point θ_f^j, the two joint caustics disappear with the trajectories generated near the maximum vector potential missing the corresponding final angle $\theta_f > \theta_f^j$, but the bifurcated caustic with $\theta_i = \pi/2$ still follows the dot-dashed green line in Fig. 4(d) until $\theta_f = \pi/2$.

At the end, we would like to point out that the temporal-caustic bifurcation is actually a universal phenomenon for all kinds of electric-field driving pulses,

which should be observable as long as the driving field is not too weak to generate a feasible angle range from θ_f^c to $\pi/2$ in an experiment. More importantly, all the dynamic properties can be easily understood by shifting and examining the momentum-space geometry following the time-dependent variation of any driving-field vector potential. Although the momentum-space geometry in Fig. 3(i) has been well established as a basic principle for the attosecond streak camera[21, 22], the caustic variation as in Fig. 4 has never been reported before.

III. PROPAGATION METHOD

A. Semiclassical propagation

Relying on the previous analysis on the classical electron dynamics, the corresponding quantum wave can be constructed quite accurately from those involved classical trajectories using a semiclassical scheme. For the time-dependent propagation, an augmented phase space is usually used by including the time t and its conjugate momentum p_t as two additional dimensions. Therefore, for our present system, the Hamiltonian governing the electron motion in the augmented phase space has the following form[20]

$$\mathcal{H}(\rho, z, t, p_\rho, p_z, p_t) = \frac{p_z^2}{2} + \frac{p_\rho^2}{2} + F(t) \cdot z + p_t \qquad (26)$$

in the cylindrical coordinate frame. Accordingly, two equations of motion are added to the standard Hamiltonian canonical equations, $dt/d\tau = 1$ and $dp_t/d\tau = -\partial \mathcal{H}/\partial t$, where τ is used as an evolution parameter for the classical trajectory propagating in the augmented phase space. In practice, it is convenient to set $t(\tau = 0) = t_i$ and $p_t(\tau = 0) = -E_0$ as two initial conditions, which guarantees $\tau = t - t_i$ and $p_t = -E(t)$ with $E(t)$ denoting the electron instantaneous energy during interaction with the field.

Starting from the initially generated outgoing wave $\psi_0(R, \theta_i, \phi_i, t_i)$ in Eq. (4), the electron wave associated with each trajectory arriving at a final point (r, θ, ϕ, t) is constructed as

$$\psi_\nu(r, \theta, \phi, t) = \psi_0(R, \theta_i, \phi_i, t_i) \cdot \mathcal{A} e^{i(\mathcal{S} - \lambda \frac{\pi}{2})}, \qquad (27)$$

where the subscript ν is used to label the corresponding trajectory. The semiclassical amplitude $\mathcal{A}$ corresponds to the local density of neighboring trajectories. $\mathcal{S}$ is the classical action accumulated in the augmented phase space. The Maslov index λ reflects the topological property of the classical trajectory from the starting point to the end point, which is naturally related to the caustics discussed above and the corresponding mathematical structures of $\mathcal{A}$ and $\mathcal{S}$ in the augmented phase space. The quantum wave $\Psi(t)$ at the final point is the coherent superposition of the semiclassical wave in Eq. (27) associated with all the possible trajectories arriving at that point.

The semiclassical amplitude can be analytically derived out as (Appendix B)

$$\mathcal{A} = \left| \frac{R^2}{k_0(t - t_i)^2 [k_0 - F(t_i)(t - t_i) \cos(\theta_i)]} \right|^{1/2} \qquad (28)$$

which is only explicitly dependent on the field strength $F(t_i)$ at the initial electron generation time t_i. The semiclassical amplitude diverges when $k_0 - F(t_i)(t - t_i) \cos(\theta_i) = 0$, which corresponds to the caustic locations as in Fig. 4(d). Therefore, the Maslov index $\lambda = 0$ when $k_0 - F(t_i)(t - t_i) \cos(\theta_i) > 0$, and $\lambda = 1$ if $k_0 - F(t_i)(t - t_i) \cos(\theta_i) < 0$.

The classical action $\mathcal{S}$ can also be obtained analytically, and its value will be extremely large for a macroscopic distance such as $r_f = 0.5 m$ considered here. However, the observable physical effect comes from the small differences between the huge phases accumulated along different trajectories. To calculate the small phase difference between each two trajectories, the following expression is used in our practical calculations (Appendix B),

$$\begin{aligned} \Delta \widetilde{\mathcal{S}} &= \widetilde{\mathcal{S}}_1 - \widetilde{\mathcal{S}}_2 \\ &= r \cdot \Pi - \frac{r}{2k_0} \cdot \Upsilon - \frac{1}{2} \int_{t_{i1}}^{t_{i2}} A^2(t') dt' \\ &\quad + A(t_{i1}) \int_{t_{i1}}^{t} A(t') dt' - A(t_{i2}) \int_{t_{i2}}^{t} A(t') dt' \end{aligned} \qquad (29)$$

where

$$\Upsilon = A^2(t_{i1}) \cdot \mu(t_{i1}) - A^2(t_{i2}) \cdot \mu(t_{i2}) ; \qquad (30)$$
$$\Pi = k_0[\mu(t_{i1}) - \mu(t_{i2})] - \cos(\theta_f)[A(t_{i1}) - A(t_{i2})] , \qquad (31)$$

and

$$\widetilde{\mathcal{S}} = \mathcal{S} - E_0 t_i , \qquad (32)$$

which has included the contributed phase from an initially outgoing wave in Eq. (4). For convenience, the arrival-time modulator $\mu(\xi, \zeta, \theta_f)$ has been denoted as $\mu(t_i)$ briefly.

With the time-dependent phase $\widetilde{\mathcal{S}}$ given by Eq. (32), the propagated wave in Eq. (27) for each trajectory can be explicitly expressed as

$$\psi_\nu(r, \theta, \phi, t) = f_L(t_i) \psi_{out}(R, \theta_i, \phi_i) \cdot \mathcal{A} e^{i(\widetilde{\mathcal{S}} - \lambda \frac{\pi}{2})} \qquad (33)$$

where the time-independent outgoing wave $\psi_{out}(R, \theta_i, \phi_i)$ is given by Eq. (2). Accordingly, the time-dependent electron flux on a spherical detector can be calculated as

$$j_r = |C(k_0)|^2 \cdot \frac{k_0^2 N_{lm}^2}{F_m r^3} \cdot \widetilde{j_r} \qquad (34)$$

where

$$N_{lm} = \sqrt{\frac{(2l+1)(l-m)!}{4\pi(l+m)!}} \qquad (35)$$

is a coefficient in the spherical harmonic function. The reduced flux $\widetilde{j}_r$ is defined as

$$\widetilde{j}_r = \Im\left[\left(\sum_\nu \widetilde{\psi}_\nu\right)^* \frac{\partial}{\partial r}\left(\sum_\nu \widetilde{\psi}_\nu\right)\right] \qquad (36)$$

following the spirit in Ref.[23]. The simplified wave function $\widetilde{\psi}_\nu$ is given by

$$\widetilde{\psi}_\nu(r,\theta,\phi,t) = \frac{\widetilde{\mathcal{A}}_\nu}{N_{lm}} \cdot Y_{lm}(\theta_i,\phi_i) \cdot e^{i(\widetilde{\mathcal{S}}_\nu - \lambda_\nu \frac{\pi}{2})} \qquad (37)$$

with the modified semiclassical amplitude expressed as

$$\widetilde{\mathcal{A}}_\nu = \frac{f_L(t_i)}{\mu(t_i)} \cdot \left|\frac{F_m r}{k_0^2 - F(t_i) \cdot r \cdot \mu(t_i) \cdot \cos(\theta_i)}\right|^{1/2}. \qquad (38)$$

Specifically, taking an s-wave source (F$^-$) for instance, the simplified wave function for each trajectory is just

$$\widetilde{\psi}_\nu^s(r,\theta,\phi,t) = \widetilde{A}_\nu e^{i(\widetilde{\mathcal{S}}_\nu - \lambda_\nu \frac{\pi}{2})}. \qquad (39)$$

If there are two trajectories arriving at the detector simultaneously as in Fig. 3(a)-(d), the electron flux from Eq. (36) has the following specific form,

$$\begin{aligned}\widetilde{j}_r =\ & p_{r_1}\widetilde{A}_1{}^2 + p_{r_2}\widetilde{A}_2{}^2 \\ & + (p_{r_1} + p_{r_2})\widetilde{A}_1\widetilde{A}_2 \cos(\Delta\varpi_{12})\end{aligned} \qquad (40)$$

with $p_r = p_\rho \sin(\theta_f) + p_z \cos(\theta_f)$, and the phase difference

$$\Delta\varpi_{12} = (S_1 - S_2) - (\lambda_1 - \lambda_2)\pi/2, \qquad (41)$$

where the derivative of $\widetilde{A}$ in Eq. (36) has been neglected owing to the same argument as in Ref.[23]. For a p_z-wave source like H$^-$, the simplified wave function for each trajectory is

$$\widetilde{\psi}_\nu^s(r,\theta,\phi,t) = \widetilde{A}_\nu \cos(\theta_i) e^{i(\widetilde{\mathcal{S}}_\nu - \lambda_\nu \frac{\pi}{2})}. \qquad (42)$$

and the corresponding electron flux can be expressed as

$$\begin{aligned}\widetilde{j}_r =\ & p_{r_1}\widetilde{A}_1{}^2 \cos^2(\theta_{i1}) + p_{r_2}\widetilde{A}_2{}^2 \cos^2(\theta_{i2}) \\ & + (p_{r_1} + p_{r_2})\widetilde{A}_1\widetilde{A}_2 \cos(\theta_{i1}) \cos(\theta_{i2}) \cos(\Delta\varpi_{12})\end{aligned} \qquad (43)$$

for two possible trajectories after replacing $\widetilde{A}_\nu$ in Eq. (40) by the combined term $\widetilde{A}_\nu \cos(\theta_i)$ including the electron initial angular distribution. For cases illustrated in Fig. 3(e) and Fig. 4, there are four trajectories arriving at the detector simultaneously in a certain region of the arrival-time plot. Therefore, there are four terms contributing to the classical flux amplitude in the first line of Eq. (40) or Eq. (43), and six terms arise in the second line, which come from interferences between each pair of two classical trajectories.

B. Quantum propagation

In this subsection, we briefly summarize the numerical procedures used in our exact quantum simulations by directly solving the time-dependent Schrödinger equation. Although the practical quantum computation turns out to be much more difficult than the above semiclassical propagation method, it is still worthwhile to make some efforts in this direction, and it answers two important questions: (1) How accurate is the above proposed semiclassical propagation scheme? (2) What will happen exactly in the classically forbidden region, especially when the temporal caustic experiences a bifurcation?

The starting point for the quantum propagation is to write the full electron wave $\Psi(t)$ as

$$\Psi(t) = \varphi_i e^{-iE_g t} + \widetilde{\Psi}(\mathbf{r},t)e^{-iE_0 t} \qquad (44)$$

where $E_g = -E_b$ with E_b denoting the binding energy of the initially bound state φ_i. The electron wave except for the initial state is represented as $\widetilde{\Psi}(\mathbf{r},t)$ with a constant phase $\exp(-iE_0 t)$ separated for convenience in practice. Substituting the above wave function into the time-dependent Schrödinger equation, one can immediately get an inhomogeneous equation as follows

$$\left[i\frac{\partial}{\partial t} - \left(H_a + H_F(t) - E_0\right)\right]\widetilde{\Psi}(\mathbf{r},t) = f(t)D\varphi_i \qquad (45)$$

under assumptions for the applied fields in Sec. II.A. The time-dependent Hamiltonian $H_F(t)$ ($= F(t) \cdot z$) on the left-hand side of Eq. (45) comes from the electron interaction with the single-cycle driving pulse. The atomic Hamiltonian $H_a = \mathbf{p}^2/2 + V(r)$ with $V(r)$ denoting the binding potential for a specific negative ion. For H$^-$, we adopt the angular-momentum-dependent model potential along with the modified dipole operator proposed in Ref. [24]. A related discussion can be found in Ref.[25] for different model potentials. For F$^-$, the model potential is taken from Ref.[26]. The initially bound state φ_i and its corresponding energy E_g can be readily obtained by diagonalizing the atomic Hamiltonian matrix in a sufficiently large radial box.

Since the initial bound state has $m = 0$ and the applied fields are also assumed to be linearly polarized (see Sec. II.A for details), the time-dependent electron wave $\widetilde{\Psi}(\mathbf{r},t)$ can be expanded as

$$\widetilde{\Psi}(\mathbf{r},t) = \frac{1}{r}\sum_l \mathcal{U}_l(r,t)Y_{l0}(\theta,\phi) \qquad (46)$$

on a two-dimensional space spanned by the discretized radial points and angular momentum basis with different l values. Using a split-operator technique, the separation of H_a from the interaction term $H_F(t)$ allows us to propagate the electron wave on each dimension independently. Therefore, the numerical propagation for each time step δt can be divided into three independent steps:

$$\widetilde{\Psi}_1 = \frac{1 - iH_F \delta t/4}{1 + iH_F \delta t/4}\widetilde{\Psi}(t) - \frac{i\delta t}{2}\varrho\left(t + \frac{\delta t}{2}\right); \qquad (47)$$

$$\widetilde{\Psi}_2 = \frac{1 - iH_a\delta t/2}{1 + iH_a\delta t/2}\widetilde{\Psi}_1 - \frac{i\delta t}{2}\varrho\left(t + \frac{\delta t}{2}\right) \quad ; \qquad (48)$$

and

$$\widetilde{\Psi}(t + \delta t) = \frac{1 - iH_F\delta t/4}{1 + iH_F\delta t/4}\widetilde{\Psi}_2 , \qquad (49)$$

where the Crank-Nicolson approximation has been used, and the notation $\varrho(t + \delta t/2)$ is used to denote briefly the source term on the right-hand side of Eq. (45). The above three steps in Eqs. (47)-(49) ensure the numerical accuracy to be $\mathcal{O}(\delta t^3)$ for each time step. For the propagation on the radial dimension in Eq. (48), a Numerov scheme is implemented on a square-root mesh[27].

Using the above Eqs. (46)-(49), we first propagate the electron wave numerically to a final time $t = 6t_w$, for which the numerical radial boundary $r_{max} = 40000$ a.u.. At the end of this propagation, the obtained wave function is projected onto all the l-dependent partial waves of H_a for each positive energy ϵ, and the corresponding expansion coefficient is calculated as

$$A_{\epsilon l} = \int \tilde{f}_{\epsilon l}(r)\mathcal{U}_l(r, t = 6t_w)dr , \qquad (50)$$

where the energy-normalized radial wave function $\tilde{f}_{\epsilon l}(r)$ can be obtained by directly integrating the stationary Schrödinger equation for H_a with specific values of ϵ and l. At a large distance such as $r = 0.5m$ we are interested here, the radial function $\tilde{f}_{\epsilon l}(r)$ behaves asymptotically in a simple form:

$$\tilde{f}_{\epsilon l}(r) = \sqrt{\frac{2}{\pi k}}\sin(kr + \vartheta_{\epsilon l}) \qquad (51)$$

with $k = \sqrt{2\epsilon}$. The asymptotic phase $\vartheta_{\epsilon l}$ includes the phase shift caused by the short-range potential $V(r)$, which can be calculated as

$$\vartheta_{\epsilon l} = \widetilde{\phi}_{\varepsilon l}(r_m) - \beta_{\epsilon l}(r_m) . \qquad (52)$$

The first part $\widetilde{\phi}_{\varepsilon l}(r_m)$ in Eq. (52) is an oscillatory phase of the computed radial function $\tilde{f}_{\epsilon l}(r)$ fitted at $r = r_m \gtrsim r_{max}$ using the sinusoidal form as in Eq. (51). The second term $\beta_{\epsilon l}(r_m)$ is a Wentzel-Kramers-Brillouin (WKB) phase correction in the asympotic region after $r = r_m$, given by

$$\beta_{\epsilon l}(r_m) = \sqrt{2\epsilon r_m^2 - l^{*2}} + l^* \arcsin\left[l^*/(kr_m)\right] \qquad (53)$$

with $l^* = l + 1/2$ following the Langer correction[28].

To calculate the electron flux on a spherical detector located at a macroscopic distance such as $0.5m$ from the photodetachment source region, we use the outgoing part in Eq. (51) and obtain the final electron outgoing wave as

$$\Psi^+(\mathbf{r}, t) = \frac{-i}{r}\sum_l Y_{l0}(\theta, \phi)\int\frac{A_{\epsilon l}}{\sqrt{2\pi k}}e^{i(kr - \epsilon t + \vartheta_{\epsilon l})}d\epsilon \quad (54)$$

which can be explicitly written out as

$$\Psi^+(\mathbf{r}, t) = \frac{-i\bar{k}}{r^{3/2}}e^{i(\frac{r^2}{2t} - \frac{\pi}{4})}\sum_l A_{\bar{\epsilon} l}e^{i\vartheta_{\bar{\epsilon} l}}Y_{l0}(\theta, \phi) \qquad (55)$$

with $\bar{k} = \sqrt{2\bar{\epsilon}} = r/t$ after using a stationary-phase approximation for the contained integration in Eq. (54). Finally, the electron flux can be immediately obtained as

$$j_r = \frac{1}{t^3} \cdot \left|\sum_l A_{\bar{\epsilon} l}e^{i\vartheta_{\bar{\epsilon} l}}Y_{l0}(\theta, \phi)\right|^2 \qquad (56)$$

from Eq. (55). One might have noticed that the second term on the right-hand side of Eq. (56) is just the angle-resolved energy spectrum. This is not a surprise, and it is actually true for any driving pulses only if the involved interaction volume and duration are negligible by comparing with the observing distance and the electron arrival time at the detector (Appendix C). Therefore, all the features discussed in this work for the time-dependent electron flux can also be expected in the angle-resolved energy spectrum. In Appendix C, a numerical verification on the accuracy of Eq. (56) is also performed by directly doing the numerical integration in Eq. (54).

IV. INTERFERENCES AND CAUSTIC BIFURCATION

Based on the electron dynamics analyzed in Sec. II. B, various different structures are expected for the classical electron arrival-time plot as in Fig. 3(a)-(e) and Fig. 4 by varying the pulse amplitude F_m or an observing angle θ_f. Using this kind of plot, one can further determine how many classical trajectories the electron follows to arrive at the detector simultaneously as in Fig. 1(a), giving an oscillatory electron flux on the detector as a function of time. Generally speaking, there are mainly three qualitatively different situations involved in all the possible arrival-time plots: two-trajectory contributed interferences, four-trajectory contributed interferences, and interferences with a temporal-caustic bifurcation. In this section, we present concrete calculations and discussions for each situation as well as the quantum tunneling effects in the classically forbidden region.

Before discussions for each specific case, we first clarify some general rules and manipulations we have used in the concrete calculations. As specified in Sec. II, we consistently assume the detecting distance is $0.5m$ as in traditional photodetachment microscopy[6], and the photoelectron initial kinetic energy $E_0 = 0.1454eV$, corresponding to a photon energy of $0.9eV$ for H$^-$. In our presented figures, the semiclassical flux was calculated using the reduced expression like Eqs. (40) and (43). For those simple cases in Fig. 2(b) and Fig. 5, a uniform approximation as in Ref.[23] has also been used near an outmost caustic. To compare with the semiclassical result, the exact quantum flux for H$^-$ given by Eq. (56) has

been scaled according to Eq. (34) with an analytic expression for $C(k_0)$ known from Ref.[10]. Note that there is no adjustable parameter between the displayed semiclassical flux and the quantum flux for H$^-$ in all figures. The displayed results for F$^-$ in Figs. 1 and 2 as well as in Figs. 5-7 have been scaled with a constant which was obtained from Fig. 2(b) by fitting the exact quantum flux for F$^-$ with that for H$^-$ at $t_f = 2.048\mu s$. The quantum flux for F$^-$ displayed in Fig. 8(c) has been fitted with the semiclassical flux at $t_f = 1.967\mu s$, and that displayed in Fig. 8(d) has been multiplied by an arbitrary constant for convenience to compare with the quantum flux for H$^-$.

For the basic interferences coming from two trajectories, a schematic demonstration has been given in Fig. 1 with $F_m = 2kV/cm$, which can be easily calculated by both the semiclassical method and the quantum approach. In contrast with the usual double-slit interferences as in traditional photodetachment microscopy[6, 10], the two trajectories in our present system are ejected at a same initial angle approximately, but their initial launch time is different as in Fig. 1(a). Besides the quantum interferences, different angle dependence can also be observed for flux amplitudes in Fig. 1(c) and (d). This can be easily understood by examining semiclassical expressions in Eq. (40) and Eq. (43), which attributes this discrepancy to the different angular distributions of the initially-generated electron wave from H$^-$ and F$^-$, respectively. The quantum fluxes from Fig. 1(c) and (d) for $\theta_f = 0$ are compared quantitatively in

Fig. 2(b), where the corresponding semiclassical flux is also displayed. The excellent agreement among different calculations further confirms the simple physical picture established by the semiclassical theory.

Figure 5 presents more examples for two-trajectory contributed interferences, where much more interference oscillations can be observed by increasing the pulse amplitude. In both Fig. 2(b) and Fig. 5, quantum fluxes for H$^-$ and F$^-$ coincide almost perfectly. This is because the electron initially-outgoing angle $\theta_i = 0$ for both the two involved trajectories with $\theta_f = 0$ (see also Fig. 3(a)). According to the semiclassical formulae in Eqs. (40) and (43), the electron flux with $\theta_i = 0$ should be exactly the same for an s-wave source (F$^-$) and a p-wave source (H$^-$) except for an energy-dependent prefactor as in Eq. (34) which has been scaled out for comparison. For the time

FIG. 6: (Color online) Interferences with possible four-trajectories involved for each arrival time t_f, where $F_m = 50kV/cm$, $r_f = 0.5m$ and $\theta_f = 0$. (a) The electron arrival-time plot reproduced from Fig. 3(e) as a reference. The corresponding semiclassical results (dotted or dashed curves) and quantum calculations (solid green curves) are shown in (b) and (c) for H$^-$ and F$^-$, respectively. Quantum fluxes for H$^-$ and F$^-$ are compared in (d) with their respective line shapes indicated in the legend. (e) The phase difference between two trajectories from the marked branches in (a).
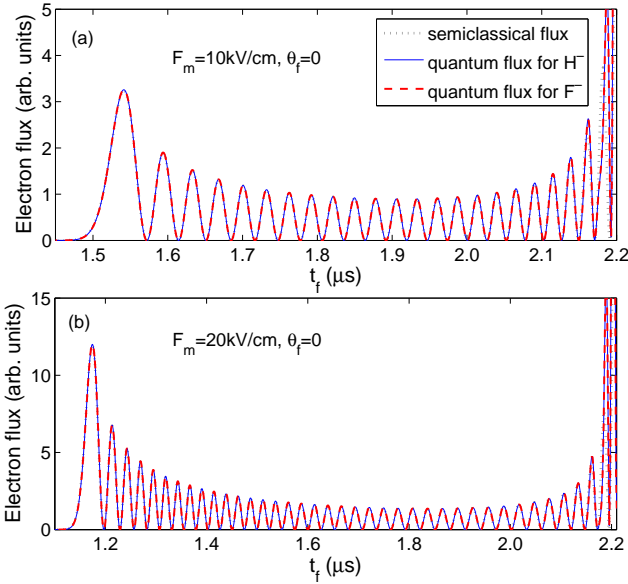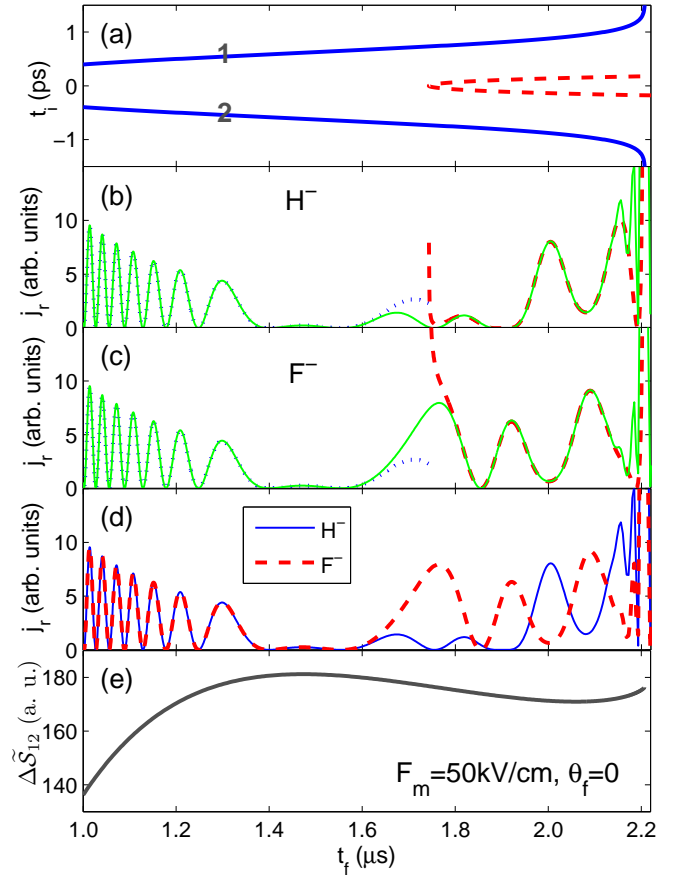

FIG. 5: (Color online) Interferences with two-trajectories involved for each arrival time t_f, where $r_f = 0.5m$ and $\theta_f = 0$. (a) $F_m = 10kV/cm$. (b) $F_m = 20kV/cm$. In both (a) and (b), the dotted line is the semiclassical result after Eq. (36), while the solid and the dashed curves are quantum calculations after Eq. (56) for H$^-$ and F$^-$, respectively.

t_f very close to $r/k_0 \approx 2.21\mu s$ in Fig. 2(b) and Fig. 5 (as well as other figures in the following), the discrepancy between the displayed semiclassical flux and exact quantum fluxes comes from two aspects: (a) the semiclassical amplitude experiences a divergence near $t_f = r/k_0$ because another temporal caustic exists according to Eq. (15) which cannot be resolved in the electron arrival-time plot as in Fig. 1(a) near $r/k_0 \approx 2.21\mu s$; (b) the background electrons near $t_f = r/k_0$ are almost unaffected by the single-cycle pulse and their effect has not been included in semiclassical calculations.

Figure 6 shows an example calculation where four-trajectory contributed interferences are involved, which corresponds to the electron arrival-time plot in Fig. 3(e) with $F_m = 50kV/cm$ and $\theta_f = 0$. We only calculated the electron flux for $t_f \geq 1\mu s$ by considering the clarity in displaying as in Fig. 6 and also the computing efficiency in quantum calculations. For the electron arrival time t_f less than $1\mu s$, it is just the basic two-trajectory contributed interferences as in Fig. 5 discussed above. For the present calculations, an excellent agreement between the quantum and semiclassical fluxes can also be observed in Fig. 6(b) and (c) for H^- and F^-, respectively, except for a small region near the temporal caustic $t_f^c = 1.743\mu s$ where the semiclassical formulas like Eqs. (40) and (43) break down. Fig. 6(d) shows a comparison between quantum fluxes for H^- and F^-. In the two-trajectory contributed region ($t_f < 1.743\mu s$), the two fluxes oscillate in pace and coincide almost perfectly, which is the same as in Fig. 2(b) and Fig. 5 we have discussed above. However, in the four-trajectory contributed region ($t_f > 1.743\mu s$), an antiphase oscillation is observed clearly between electron fluxes from H^- and F^-. This can also be understood quite well from the semiclassical picture. The initially outgoing angle $\theta_i = 0$ for trajectories from the solid blue line in the electron arrival-time plot (Fig. 6(a)) while $\theta_i = \pi$ for trajectories from the dashed red curve in Fig. 6(a). According to the semiclassical formulae, the interference term contributed by trajectories with $\theta_i = 0$ and $\theta_i = \pi$ has an initial-angle dependent factor $[\cos(0)\cos(\pi)] = -1$ in Eq. (43) for a p_z-wave source like H^-, which reverses the oscillatory behavior with respect to the interference term in Eq. (40) for an s-wave source like F^-.

Another two interesting observations are related to the oscillation amplitude and phase of the electron flux in different time ranges. In the two-trajectory contributed region, only the initial launch time is slightly different for the two involved trajectories whose initially-outgoing angles are approximately the same. As a consequence, they almost follow a same classical orbit except for a tiny difference between their evolution duration. Therefore, the semiclassical amplitudes $\mathcal{A}_1$ and $\mathcal{A}_2$ are approximately equal. According to Eqs. (40) and (43), an approximate zero value can be touched as in Fig. 2(b), Fig. 5 and Fig. 6, when $\cos(\Delta\varpi_{12}) = -1$ (note $p_{r_1} \approx p_{r_2}$ in our current system). However, in the four-trajectory contributed region, the finite minimum values are observed clearly in
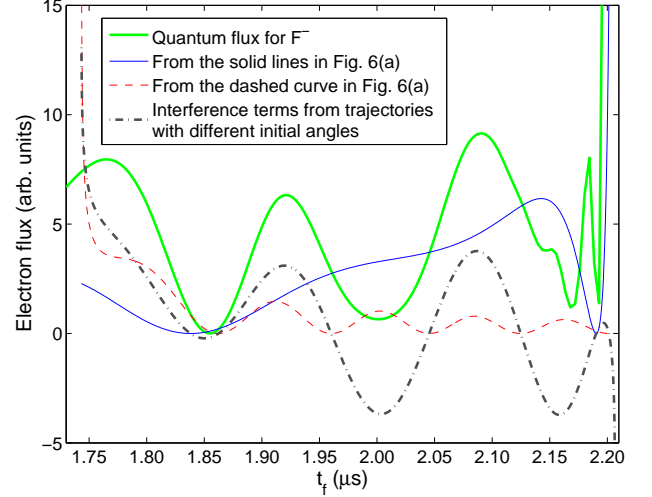

FIG. 7: (Color online) Analysis for the four-trajectory contributed region in Fig. 6 by taking F^- for instance. The bold solid green curve is the quantum flux for F^-, which is reproduced from Fig. 6(c) as a reference. The thin solid blue curve is the semiclassical flux contributed by the two trajectories from the solid blue lines in Fig. 6(a) with $\theta_i = 0$, and the dashed red curve presents the semiclassical contributions by the two trajectories from the dashed red curve in Fig. 6(a) with $\theta_i = \pi$. The bold dot-dashed line shows the contribution of the other four terms in the semiclassical-flux expression coming from the quantum interferences between those trajectories with different initial angles.

Fig. 6 for the oscillatory fluxes. To understand this, we divide the semiclassical-flux expression into three parts as in Fig. 7 by taking F^- for instance. From Fig.7, one can immediately find that the electron flux from the two trajectories with $\theta_i = 0$ only experiences one oscillation between $1.85\mu s$ and about $2.2\mu s$ (see the following discussion for the phase difference), and its large positive value is the main reason for the finite minimum flux in Fig. 6. Another necessary condition is that the electron-wave amplitude from $\theta_i = \pi$ should be small enough to guarantee the interference oscillations from the dashed and the dot-dashed curves in Fig. 7 cannot offset the large positive contribution from the two trajectories with $\theta_i = 0$. The physical picture for the small electron-wave amplitude as indicated by the dashed curve in Fig.7 is that the two trajectories with $\theta_i = \pi$ initially propagate in a completely opposite direction relative to another two trajectories with $\theta_i = 0$, and their neighboring trajectories finally turn out to be more divergent.

The phase difference $\Delta\widetilde{\mathcal{S}}_{12}$ is also shown in Fig. 6(e) for the two indicated trajectories in Fig. 6(a), which explains why the oscillation frequency varies dramatically in the time range shown in Fig. 6. For $t_f \lesssim 1.2\mu s$, the phase difference $\Delta\widetilde{\mathcal{S}}_{12}$ almost changes monotonically with the time t_f, giving an approximate uniform oscillation for the electron flux. In contrast, for $t_f \gtrsim 1.2\mu s$, the

phase difference between these two trajectories hardly change with the different time t_f. Therefore, the electron flux contributed by the two trajectories with $\theta_i = 0$ oscillates slowly as in Fig. 6 and also the thin solid curve in Fig. 7, and the oscillatory behavior observed in the four-trajectory contributed region is mainly contributed by the interferences between trajectories with different initial angles, which is illustrated by the bold dot-dashed curve in Fig. 7. Especially, near its extremum at $t_f \sim 1.5\mu s$, the phase difference $\Delta\widetilde{\mathcal{S}}_{12}$ varies slowly around the value of $180 \sim (56 + 3/2)\pi$. As a consequence, $\cos(\Delta\varpi_{12}) = \cos(\Delta\widetilde{\mathcal{S}}_{12} - \pi/2) \approx -1$ in Eqs. (40) and (43), which explains the oscillation-amplitude suppression observed near $t_f = 1.5\mu s$ in Fig. 6(b)-(d).

Figure 8 is a representative case for quantum interferences with a temporal-caustic bifurcation, which corresponds to the electron arrival-time plot in Fig. 4(b) with $F_m = 20kV/cm$ and $\theta_f = \pi/3$. By just observing the classical arrival-time plot as in Fig. 8(a), it is similar to Fig. 6 in that both the two-trajectory and four-trajectory contributed interferences are involved, but the resulted electron flux still has several different interesting features. Quantum fluxes for H^- and F^- are compared in Fig. 8(d) between each other. It can also be observed
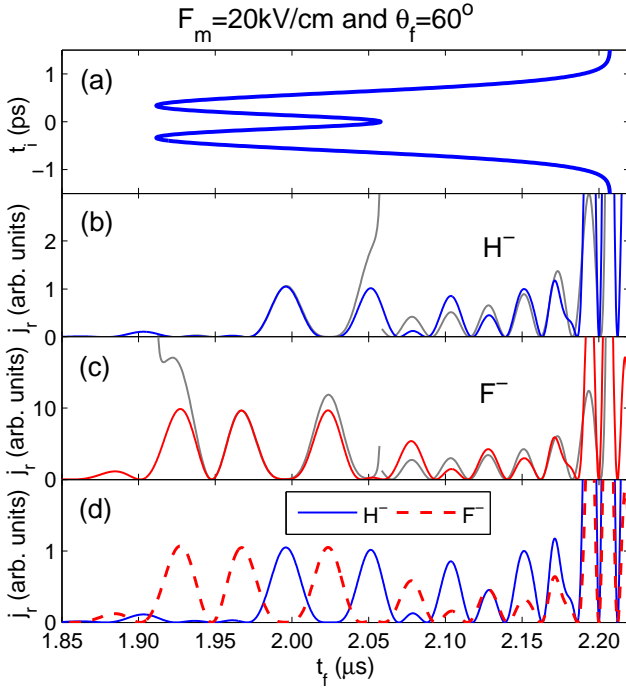

FIG. 8: (Color online) Interferences with a temporal-caustic bifurcation occurred, where $F_m = 20kV/cm$, $r_f = 0.5m$ and $\theta_f = \pi/3$. (a) The electron arrival-time plot reproduced from Fig. 4(b) as a reference. The corresponding semiclassical results (solid gray lines) and quantum calculations (heavy solid and colored curves) are shown in (b) and (c) for H^- and F^-, respectively. Quantum fluxes for H^- and F^- are compared in (d) with their respective line shapes indicated in the legend.

that the fluxes from H^- and F^- oscillate antiphase in the four-trajectory contributed region while oscillating in pace in the two-trajectory contributed region, which is similar to those observations in Fig. 6(d). Nevertheless, there are two new features appeared in Fig. 8(d): (a) the flux amplitude for H^- almost vanishes near the newly-born caustic near $t_f = 1.912\mu s$. This is because the initially generated outgoing p-wave from H^- has a node near $\theta_i = \pi/2$, and the electron flux is therefore largely suppressed near $t_f = 1.912\mu s$ with its contributed trajectories having initial angles near $\theta_i = \pi/2$ (Fig. 4(b) and (c)). (b) the electron fluxes for H^- and F^- do not coincide any more in the two-trajectory contributed region, which can be easily understood by realizing that initial angles for the contributed trajectories are no longer the same as in Fig. 6 for different time t_f.

By comparing the semiclassical flux and the quantum flux in Fig. 8(b) and (c) for H^- and F^-, respectively, only a good agreement can be found in the four-trajectory contributed region. Near the two temporal caustics, the semiclassical flux diverges as usual, and the divergent property of the semiclassical amplitude for H^- is suppressed by the factor $\cos(\theta_i)$ as in Eq. (43) with the initial angle θ_i tends to $\pi/2$ when the final time t_f approaches the caustic near $t_f = 1.912\mu s$. In the classically-forbidden region with $t_f \lesssim 1.912\mu s$, an interference oscillation can still be observed as the quantum-tunneling effect from the two extrema near $t_f = 1.912\mu s$. In the two-trajectory contributed region, the oscillation phase is almost the same between the quantum flux and semiclassical calculations, but an obvious discrepancy exists for the flux amplitude, which can also be attributed to a quantum tunneling effect of the electron wave near the temporal caustic at $t_f = 2.058\mu s$. This quantum tunneling wave interferes with the two wave parts contributed by the two classical trajectories, resulting two observable effects in Fig. 8(b) and (c): (a) the semiclassical-flux amplitude associated with the two classical trajectories (gray curves) is modulated peak by peak as shown by the heavy sold curves; (b) the amplitude modulation caused by this quantum-tunneling wave is antiphase for H^- and F^- as those interferences in the four-trajectory contributed region.

At the end of this discussion, we would like to point out that all the observed structures above could also be observable in the angle-resolved electron energy spectrum according to an equivalence expressed in Eq. (C6). In a real experiment, one may need to determine whether the time-dependent electron flux or the angle-resolved energy spectrum can be easily measured with a satisfying resolution. One more important feature related to the temporal-caustic bifurcation is that the earliest time t_f for the electron flux to be detected is approximately determined by the newly-born temporal caustic like $t_f = 1.912\mu s$ in Fig. 4(b) and Fig. 8, which is fixed and does not change for different field amplitudes F_m, indicated by the dot-dashed green line in Fig. 4(d) and given by $r_f \sin(\theta_f)/k_0$ at a specific angle θ_f. Accord-

ingly, a maximum energy value of $k_0^2 \csc^2(\theta_f)/2$ exists in the angle-resolved energy spectrum no matter how strong the applied driving pulse field is, as long as the temporal caustic experiences a bifurcation.

In addition, for all the above analysis and discussions, we assumed the weak laser field applied for initiating the electron wave is linearly polarized, and the initially outgoing wave generated from H^- has a zero angular-momentum component on the z-direction of the laser polarization. However, if a circularly-polarized laser light is used, an electron outgoing wave with $m = 1$ can be generated. In contrast with the current situation we considered with $m = 0$, the electron can rotate around the z-axis during its interaction with a single-cycle driving pulse, therefore more interesting effects can be expected, which should also be an interesting direction in the future investigations.

V. CONCLUSION

Inspired by the recent availability of a single-cycle pulse in experiments (see, *e.g.* Ref.[3]), we demonstrated a possible application of a single-cycle driving pulse in modulating and controlling the photodetachment dynamics of negative ions. The involved electron dynamics for different pulse amplitudes can be classified and examined by different topological geometries in the corresponding momentum space. A universal temporal-caustic bifurcation has been observed when the observing angle deviates away from the field-polarization direction. Combining with the electron arrival-time plot together, we found that the electron can follow two or more classical trajectories to arrive at a detector simultaneously, thereby giving an oscillatory electron flux in the real-time domain as a result of quantum interferences. By comparing the electron fluxes for H^- and F^-, both the inphase and antiphase oscillations have been observed, depending on the pulse amplitude and the observing angle.

With the detector far away from the photodetachment zone, the number of interference oscillations does not change, which has been already determined in the temporal-spatial volume for interacting with the short driving pulse. In contrast, the oscillation period increases with the detecting distance, which makes the interference pattern much easier to be resolved at a larger distance. However, the electron signal will be weaker by increasing the observing distance. As a consequence, there is a balance between the detector sensitivity in an experiment and increasing the detecting distance for a higher resolution. In our calculations, we assumed the detecting distance to be $0.5m$ as in traditional photodetachment microscopy. A macroscopic distance less than this value should also be feasible, especially for the electron flux at $\theta_f = 0$ with a sufficiently strong driving pulse, unless a highly accuracy was desired.

Although our current work was mainly about the photodetachment of atomic negative ions and a single-cycle driving pulse, the involved general picture as well as its related formulae developed here could be easily extended and applied for other similar systems where the electron experiences an interaction with an applied electric-field driving pulse. The time-dependent electron flux investigated here has been established as an equivalence of the angle-resolved electron energy spectrum at large distances which is usually concerned in the strong field and ultrafast physics[15–17, 21, 22]. Moreover, the temporal-caustic bifurcation as a universal phenomenon should also have some interesting effects in other similar systems. On the other hand, the present idea could also be directly applied for neutral atoms instead of negative ions here, by including the long-range Coulomb potential, which can be seen as an extension of traditional photoionization microscopy in the time domain.

Appendix A: SOLVING THE CLASSICAL ELECTRON-ORBIT EQUATION

First, the integrals of $A(t)$ and $A^2(t)$ can be analytically written out as follows,

$$\int_{t_1}^{t_2} A(t)dt$$
$$= -\frac{F_m t_w^2}{2}\sqrt{\frac{\pi e}{2}}\left[\mathrm{erf}\left(\frac{t_2}{t_w}\right) - \mathrm{erf}\left(\frac{t_1}{t_w}\right)\right] ; \quad (A1)$$

and

$$\int_{t_1}^{t_2} A^2(t)dt$$
$$= \frac{F_m^2 t_w^3 e}{4}\sqrt{\frac{\pi}{2}}\left[\mathrm{erf}\left(\frac{\sqrt{2}t_2}{t_w}\right) - \mathrm{erf}\left(\frac{\sqrt{2}t_1}{t_w}\right)\right] , (A2)$$

in terms of the standard error function $\mathrm{erf}(x)$. These two integrals will be involved in this appendix and next one, respectively. From Eq. (A1), the field-induced displacement $\Delta\tilde{z}(t_i)$ has the following form,

$$\Delta\tilde{z}(t_i) = -\frac{F_m t_w^2}{2}\sqrt{\frac{\pi e}{2}}\left[1 - \mathrm{erf}\left(\frac{t_i}{t_w}\right)\right] . \qquad (A3)$$

Combining Eq. (10) and Eq. (14), a quadratic equation can be obtained for $\tau = t - t_i$,

$$\tilde{a}(t - t_i)^2 + \tilde{b}(t - t_i) + \tilde{c} = 0 \qquad (A4)$$

with

$$\tilde{a} = A^2(t_i) - k_0^2 ; \qquad (A5)$$
$$\tilde{b} = 2A(t_i)[r_f \cos(\theta_f) - \Delta\tilde{z}(t_i)] ; \qquad (A6)$$
$$\tilde{c} = r_f^2 + [\Delta\tilde{z}(t_i)]^2 - 2r_f \cos(\theta_f)\Delta\tilde{z}(t_i) . \qquad (A7)$$

where $z(t_f) = r_f \cos(\theta_f)$ is used and $\tilde{c}$ is always positive.

For $-A(t_i) < k_0$, $\tilde{a} < 0$, and Eq. (A4) has and only has one positive solution satisfying the physical requirement, for which the arrival-time modulator $\mu(\xi, \zeta, \theta_f)$ in Eq. (15) can be solved as

$$\mu(\xi, \zeta, \theta_f) = \frac{\Xi - \sqrt{\Lambda}}{\xi^2 - 1} \; ; \qquad \xi < 1 \qquad \text{(A8)}$$

with $\xi = -A(t_i)/k_0$ and $\zeta = \Delta\tilde{z}(t_i)/r_f$ as defined below Eq. (15), and

$$\Xi = \xi[\cos(\theta_f) - \zeta] \; ; \qquad\qquad\qquad \text{(A9)}$$
$$\Lambda = [1 + \zeta^2 - 2\zeta\cos(\theta_f)] - \xi^2\sin^2(\theta_f) \; . \quad \text{(A10)}$$

When $\theta_f = 0$ and $\theta_f = \pi$, respectively, Eq. (A8) can be further simplified as

$$\mu(\xi, \zeta, \theta_f = 0) = \frac{k_0}{k_0 + [-A(t_i)]} \cdot \left[1 - \frac{\Delta\tilde{z}(t_i)}{r_f}\right] \quad \text{(A11)}$$

and

$$\mu(\xi, \zeta, \theta_f = \pi) = \frac{k_0}{k_0 - [-A(t_i)]} \cdot \left[1 + \frac{\Delta\tilde{z}(t_i)}{r_f}\right] \; , \quad \text{(A12)}$$

where $k_0 + [-A(t_i)]$ and $k_0 - [-A(t_i)]$ are actually the electron final momenta k_f in each case after interacting with the applied pulse field.

For $-A(t_i) > k_0$, $\tilde{a} > 0$ and $\tilde{b} < 0$. The existence of solutions is determined by the following discriminant,

$$\Delta = \tilde{b}^2 - 4\tilde{a}\tilde{c} \geq 0 \; , \qquad\qquad \text{(A13)}$$

which gives a maximum angle θ_f^m the electron can finally reach on a spherical detector located at a distance r_f from the source region,

$$\theta_f^m = \arccos\left\{\frac{1}{\xi^2} \cdot \left[\zeta + \sqrt{(1 - \xi^2)(\zeta^2 - \xi^2)}\right]\right\} \; . \quad \text{(A14)}$$

There are two solutions for $\theta_f < \theta_f^m$,

$$\mu_<(\xi, \zeta, \theta_f) = \frac{\Xi - \sqrt{\Lambda}}{\xi^2 - 1} \; , \qquad\qquad \text{(A15)}$$

$$\mu_>(\xi, \zeta, \theta_f) = \frac{\Xi + \sqrt{\Lambda}}{\xi^2 - 1} \; , \qquad \xi > 1 \; . \quad \text{(A16)}$$

Where the subscripts of μ indicate that $\mu_<$ is smaller than $\mu_>$. When $\theta_f = \theta_f^m$, $\Lambda = 0$ and

$$\mu_<(\xi, \zeta, \theta_f^m) = \mu_>(\xi, \zeta, \theta_f^m) = \frac{\xi[\cos(\theta_f^m) - \zeta]}{\xi^2 - 1} \; . \quad \text{(A17)}$$

At $\theta_f = 0$,

$$\mu_<(\xi, \zeta, \theta_f = 0) = \frac{k_0}{[-A(t_i)] + k_0} \cdot \left[1 - \frac{\Delta\tilde{z}(t_i)}{r_f}\right] \quad \text{(A18)}$$

corresponds to $\theta_i = 0$, and

$$\mu_>(\xi, \zeta, \theta_f = 0) = \frac{k_0}{[-A(t_i)] - k_0} \cdot \left[1 - \frac{\Delta\tilde{z}(t_i)}{r_f}\right] \quad \text{(A19)}$$

corresponds to $\theta_i = \pi$. There is no corresponding classical trajectory for $\theta_f > \theta_f^m$.

For $-A(t_i) = k_0$, $\tilde{a} = 0$ in Eq. (A4), and the requirement of a positive value of $t - t_i$ gives a classical boundary

$$\theta_f^m = \arccos\left[\frac{\Delta\tilde{z}(t_i)}{r_f}\right] \qquad\qquad \text{(A20)}$$

for the electron final angle on the spherical detector placed at a distance r_f. For $\theta_f < \theta_f^m$, the arrival-time modulator $\mu(\xi, \zeta, \theta_f)$ in Eq. (15) turns out to be

$$\mu(\xi, \zeta, \theta_f) = \frac{1 - \zeta^2}{2[\cos(\theta_f) - \zeta]} - \zeta \; , \qquad \xi = 1 \; . \quad \text{(A21)}$$

which goes to $+\infty$ when $\theta_f = \theta_f^m$. For $\theta_f = 0$, the above expression can be simplified as

$$\mu(\xi, \zeta, \theta_f = 0) = \frac{1}{2}\left[1 - \frac{\Delta\tilde{z}(t_i)}{r_f}\right] \qquad \text{(A22)}$$

which is a continuation of Eq. (A11) and Eq. (A18) at $A(t_i) = k_0$.

Appendix B: SEMICLASSICAL AMPLITUDE AND PHASE ACCUMULATION

Quantitatively, the semiclassical amplitude $\mathcal{A}$ is described as

$$\mathcal{A}(t) = \left|\frac{J(\tau = 0)}{J(\tau = t - t_i)}\right|^{1/2} \qquad\qquad \text{(B1)}$$

by the time-dependent Jacobian $J(\tau)$ at the final point compared with its initial value at the starting point. The specific form of $J(\tau)$ in the cylindrical coordinate can be defined as

$$J(\tau) = \rho \cdot \det\left(\frac{\partial(\rho, z, t)}{\partial(t_i, \theta_i, \tau)}\right) \; . \qquad\qquad \text{(B2)}$$

which can be further simplified as

$$J(\tau) = \rho \cdot \left(\frac{\partial\rho}{\partial t_i}\right)_{\theta_i, t} \cdot \left(\frac{\partial z}{\partial\theta_i}\right)_{\rho, t} \qquad\qquad \text{(B3)}$$

by combining the reduction procedures in Appendices of Refs.[20, 23]. Note the derivative $dr/d\theta$ in Eqs. (B6) and (B7) of Ref.[23] should be $(\partial r/\partial\theta)_t$, since the variable t was missed in Eq. (B5) there.

For the initially outgoing spherical wave, one can readily show that

$$J(\tau = 0) = k_0 R^2 \sin(\theta_i) \; . \qquad\qquad \text{(B4)}$$

For the electron propagation driven by a single-cycle pulse, the partial derivative of ρ with respect to t_i in Eq. (B3) can be easily obtained from Eq. (10). The partial derivative of z with respect to θ_i is given by the following relationship,

$$\left(\frac{\partial z}{\partial \theta_i}\right)_{\rho,t} = \left(\frac{\partial z}{\partial \theta_i}\right)_{t_i,t} + \left(\frac{\partial z}{\partial t_i}\right)_{\theta_i,t} \cdot \left(\frac{\partial t_i}{\partial \theta_i}\right)_{\rho,t} \quad \text{(B5)}$$

where all the partial derivatives on the right-hand side can be already obtained analytically from Eq. (11). Therefore, the final expression as in Eq. (28) can be derived for the semiclassical amplitude, by combining the above equations and using the partial derivatives from Eqs. (10) and (11).

Similar to the standard definition in the usual phase space, the classical action $\mathcal{S}$ in the augmented phase space is given by the following integral along all the canonical variables,

$$\mathcal{S} = \int p_\rho d\rho + p_z dz + p_t dt , \quad \text{(B6)}$$

which turns out to be

$$\mathcal{S} = \frac{1}{2}\int p_\rho^2 dt + \frac{1}{2}\int p_z^2 dt - \int F(t)z(t)dt \quad \text{(B7)}$$

following the generalized Hamiltonian in Eq. (26). The last integral in the above equation can be separated as

$$-\int F(t)z(t)dt = z(t)\cdot\Delta p_z(t) - \int [\Delta p_z(t)]\cdot p_z(t)dt \quad \text{(B8)}$$

after integration by parts using the impulse momentum theorem. Substituting Eq. (B8) into Eq. (B7) and using $\Delta p_z(t) = p_z(t) - p_z(t_i)$, the classical action $\mathcal{S}$ can be explicitly written as

$$\mathcal{S} = E_0(t-t_i) + z(t)\cdot\Delta p_z(t) - \frac{1}{2}\int [\Delta p_z(t)]^2 dt \quad \text{(B9)}$$

with $\Delta p_z(t) = A(t) - A(t_i)$ as in Eq. (12), where the involved integrals of $A(t)$ and $A^2(t)$ are given by Eqs. (A1) and (A2). By further including an initial phase of the generated electron wave at t_i as in Eq. (32), and using the formal expression in Eq. (15) for the relationship between t and t_i, the phase difference in Eq. (29) can be obtained after a simple rearrangement.

Appendix C: NUMERICAL VERIFICATION ON THE ACCURACY OF EQ.(56)

The simple form in Eq. (56) for the flux calculation benefits from the stationary-phase approximation used for the integration in Eq. (54). Here, we first demonstrate that the simple expression in Eq. (56) is quite accurate by directly doing the numerical integration in Eq. (54), and then a general argument will be presented
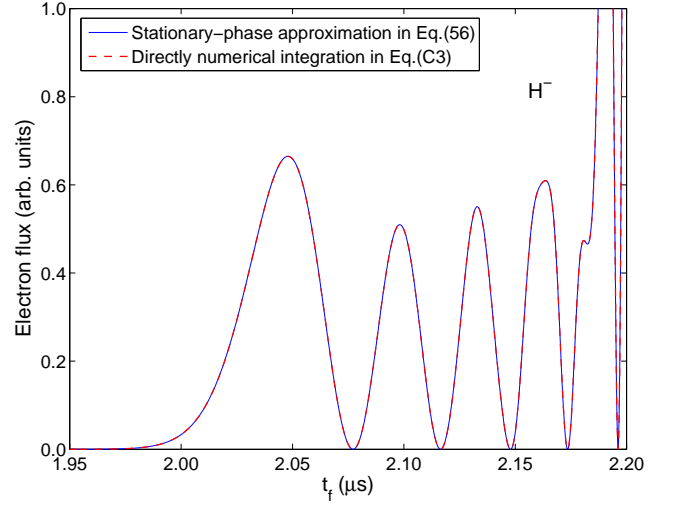

FIG. 9: (Color online) Numerical verification on the accuracy of the simple expression in Eq. (56). The solid curve is calculated after Eq. (56) for H$^-$ with $F_m = 2kV/cm$, $r_f = 0.5m$ and $\theta_f = 0$. The dashed curve is given by Eq. (C3) by directly doing the numerical integrations in Eqs. (C1) and (C2).

for the simple relationship between the time-dependent electron flux and the angle-resolved energy spectrum.

For convenience, we first define two integrals as follows,

$$I_{lt}^0 = \int \frac{A_{\epsilon l}}{\sqrt{k}}e^{i\vartheta_{\epsilon l}}e^{-it(\sqrt{\epsilon}-\sqrt{\bar{\epsilon}})^2}d\epsilon ; \quad \text{(C1)}$$

$$I_{lt}^1 = \int \sqrt{k}A_{\epsilon l}e^{i\vartheta_{\epsilon l}}e^{-it(\sqrt{\epsilon}-\sqrt{\bar{\epsilon}})^2}d\epsilon , \quad \text{(C2)}$$

which allows us to write down the electron flux as

$$j_r = \frac{1}{2\pi r^2}\sum_{ll'}\Re(I_{lt}^{0*}I_{l't}^1)Y_{l0}(\theta,\phi)Y_{l'0}(\theta,\phi) \quad \text{(C3)}$$

after Eq. (54), where $\Re$ means the real part of its variable. The two integrands in Eqs. (C1) are (C2) are highly oscillatory when the energy is slightly deviating away from the stationary point $\bar{\epsilon} = r^2/(2t^2)$, because the final time t is on the scale of microsecond which is an extremely large number in atomic units. In order to handle this integration, a gaussian-shape window function $W(\epsilon) = exp[-((\epsilon-\bar{\epsilon})/\Delta\epsilon)^2]$ is multiplied to the integrand in our practical numerical integration, which provides an accurate and well-convergent result for the integration as long as the window is sufficiently wide to cover enough number of oscillation cycles in the concerned integrand.

Assuming $t(\sqrt{\epsilon} - \sqrt{\bar{\epsilon}})^2 = \pi$, we get an estimation for a reference energy-width $\Delta\epsilon_0$ as

$$\Delta\epsilon_0 = \sqrt{16\pi\bar{\epsilon}/t} \quad \text{(C4)}$$

during which the integrand experiences one full cycle approximately. In practice, we use $\Delta\epsilon = 10\Delta\epsilon_0$ with $\Delta\epsilon_0$ given by Eq. (C4) at the earliest electron arrival time.

For the demonstrated case in Fig. 9, $t = 1.95\mu s$ is used in Eq. (C4) to determine the reference width $\Delta\epsilon_0$. The actual numerical integration can be made from $\bar{\epsilon} - 6\Delta\epsilon$ to $\bar{\epsilon} + 6\Delta\epsilon$ for each final time t. Figure 8 shows a comparison between electron fluxes obtained, respectively, from Eq. (56) and the directly numerical integration as in Eqs. (C1)-(C3). The almost perfect coincidence between the two calculations in Fig. 9 indicates that the stationary-phase approximation works very well at least for our current case, and the simple expression in Eq. (56) is accurate enough.

To understand why the time-dependent electron flux is simply related to the angle-resolved energy spectrum as in Eq. (56), one can imagine that the total photodetachment probability P should be the same whether you calculate it by integrating the electron flux or the energy spectrum, that is

$$
\begin{aligned}
P &= \int j_r r^2 \sin\theta d\theta d\phi dt \\
&= \int \left(\frac{dP}{\sin\theta d\theta d\phi d\epsilon} \right) \sin\theta d\theta d\phi d\epsilon \ . \quad \text{(C5)}
\end{aligned}
$$

For any driving pulses, if the observing distance r is much larger than the spatial range of the electron-field interaction, and the interaction duration is also much shorter than the final time t for the electron to arrive at the detector, then the electron velocity can be given by r/t quite accurately, and accordingly $\epsilon = r^2/(2t^2)$ holds in atomic units, which is just the stationary-phase point for the integration in Eq. (54). Following this line, we get $d\epsilon = -r^2 dt/t^3$ which gives us

$$
j_r = \frac{1}{t^3} \cdot \left(\frac{dP}{\sin\theta d\theta d\phi d\epsilon} \right) \quad \text{(C6)}
$$

by substituted into Eq. (C5). Therefore, in this sense, our studied time-dependent electron flux are equivalent to the angle-resolved energy spectrum.

[1] S. Fleischer, Y. Zhou, R. W. Field, and K. A. Nelson, Phys. Rev. Lett. **107**, 163603 (2011).
[2] K. N. Egodapitiya, S. Li, and R. R. Jones, Phys. Rev. Lett. **112**, 103002 (2014).
[3] S. Li and R. R. Jones, Phys. Rev. Lett. **112**, 143006 (2014).
[4] B. C. Yang and F. Robicheaux, Phys. Rev. A **90**, 063413 (2014).
[5] B. C. Yang and F. Robicheaux, Phys. Rev. A **91**, 043407 (2015).
[6] C. Blondel, C. Delsart and F. Dulieu, Phys. Rev. Lett. **77**, 3755 (1996).
[7] C. Delsart, F. Goldfarb, and C. Blondel, Phys. Rev. Lett. **89**, 183002 (2002).
[8] I. I. Fabrikant, Sov. Phys.-JETP **52**, 1045 (1980).
[9] Y. N. Demkov, V. D. Kondratovich and V. N. Ostrovskii, JETP Lett. **34**, 403 (1981).
[10] M. L. Du, Phys. Rev. A **40**, 4983 (1989).
[11] C. Nicole, H. L. Offerhaus, M. J. J. Vrakking, F. Lépine, and C. Bordas, Phys. Rev. Lett. 88, 133001 (2002).
[12] S. Cohen, M. M. Harb, A. Ollagnier, F. Robicheaux, M. J. J. Vrakking, T. Barillot, F. Lépine, and C. Bordas, Phys. Rev. Lett. **110**, 183001 (2013).
[13] A. S. Stodolna, A. Rouzee, F. Lépine, S. Cohen, F. Robicheaux, A. Gijsbertsen, J. H. Jungmann, C. Bordas, and M. J. J. Vrakking, Phys. Rev. Lett. **110**, 213001 (2013).
[14] A. S. Stodolna, F. Lépine, T. Bergeman, F. Robicheaux, A. Gijsbertsen, J. H. Jungmann, C. Bordas, and M. J. J. Vrakking, Phys. Rev. Lett. **113**, 103002 (2014).
[15] F. Lindner, M. G. Schätzel, H. Walther, A. Baltuška, E. Goulielmakis, F. Krausz, D. B. Milošević, D. Bauer, W. Becker, and G. G. Paulus, Phys. Rev. Lett. **95**, 040401 (2005).
[16] T. Remetter, P. Johnsson, J. Mauritsson, K. Varjú, Y. Ni, F. Lépine, E. Gustefsson, M. Kling, J. Khan, R. López-Martens, K. J. Schafer, M. J. J. Vrakking and A. L'huillier, Nature Physics **2**, 323 (2006).
[17] F. O. Kirchner, A. Gliserin, F. Krausz, and P. Baum, Nature Photonics **8**, 52 (2014).
[18] N. L. Manakov, M. V. Frolov, A. F. Starace, and I. I. Fabrikant, J. Phys. B: At. Mol. Opt. Phys. **33** R141 (2000) and references therein.
[19] E. P. Wigner, Phys. Rev. **73**, 1002 (1948).
[20] M. R. Haggerty and J. B. Delos, Phys. Rev. A **61**, 053406 (2000).
[21] M. Hentschel, R. Kienberger, C. Spielmann, G. A. Reider, N. Milošević, T. Brabec, P. Corkum, U. Heinzmann, M. Drescher, and F. Krausz, Nature **414**, 509 (2001).
[22] J. Itatani, F. Quéré, G. L. Yudin, M. Yu. Ivanov, F. Krausz, and P. B. Corkum, Phys. Rev. Lett. **88**, 173903 (2002).
[23] B. C. Yang, J. B. Delos, and M. L. Du, Phys. Rev. A **88**, 023409 (2013).
[24] C. Laughlin and S. I. Chu, Phys. Rev. A **48**, 4654 (1993).
[25] K. Krajewska, I. I. Fabrikant, and A. F. Starace, Phys. Rev. A **74**, 053407 (2006).
[26] X. X. Zhou, Z. J. Chen, T. Morishita, A. T. Le, and C. D. Lin, Phys. Rev. A **77**, 053410 (2008).
[27] F. Robicheaux, J. Phys. B: At. Mol. Opt. Phys. **45**, 135007, (2012).
[28] R. E. Langer, Phys. Rev. **51**, 669 (1937).